NANO LETTERS

pubs.acs.org/NanoLett Letter

Ultrafast Synthesis of Oxygen Vacancy-Rich $MgFeSiO_4$ Cathode to Boost Diffusion Kinetics for Rechargeable Magnesium-Ion Batteries

Jie Xu, Yuqi Hong, Shuming Dou, Junhan Wu, Jingchao Zhang, Qingmeng Wang, Tiantian Wen, Yang Song, Wei-Di Liu, Jianrong Zeng, Guangsheng Huang,* Chaohe Xu, Yanan Chen,* Jili Yue,* Jingfeng Wang, and Fusheng Pan

Cite This: https://doi.org/10.1021/acs.nanolett.4c04908 Read Online

ACCESS | Metrics & More | Article Recommendations | Supporting Information

ABSTRACT: Rechargeable magnesium ion batteries (RMBs) have drawn extensive attention due to their high theoretical volumetric capacity and low safety hazards. However, divalent Mg ions suffer sluggish mobility in cathodes owing to the high charge density and slow insertion/extraction kinetics. Herein, it is shown that an ultrafast nonequilibrium high-temperature shock (HTS) method with a high heating/quenching rate can instantly introduce oxygen vacancies into the olivine-structured $MgFeSiO_4$ cathode ($MgFeSiO_4$-HTS) in seconds. As a proof of concept, the $MgFeSiO_4$-HTS exhibits a higher electrochemical property and fast insertion/extraction kinetics in comparison to those prepared from the conventional sintering method. The $MgFeSiO_4$-HTS displays remarkable long-term cycling lifespan properties with a reversible capacity of 85.65 and 54.43 mAh g^{-1} over 500 and 1600 cycles at 2 and 5 C, respectively. Additionally, by combining the electrochemical experiments and density functional theory calculations, oxygen vacancies can weaken the interaction and energy barrier between the Mg^{2+} ions and the cathode, enhancing the Mg^{2+} diffusion kinetics.

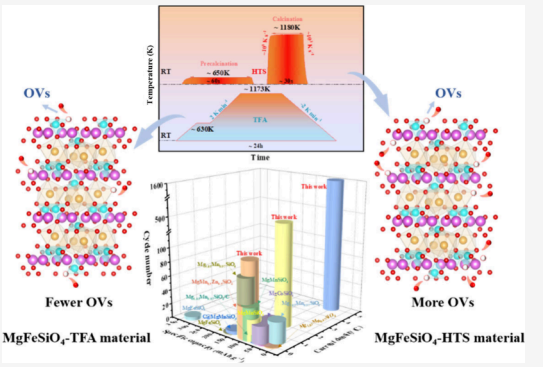

KEYWORDS: *Rechargeable magnesium ion batteries, Olivine-structured $MgFeSiO_4$, High-temperature shock technology, Defect engineering, Mg^{2+} and $MgCl^+$ cointercalation*

Rechargeable magnesium ion batteries (RMBs) have been extensively considered as next-generation energy storage technology beyond lithium-ion batteries (LIBs) due to the abundant Mg natural abundance, the high theoretical volumetric capacity (3833 mAh cm^{-3}), and the relatively low reduction potential (−2.37 V versus the standard hydrogen electrode).[1−4] Moreover, Mg metal as the anode has a dendrite-free deposition at normal current densities in most RMBs electrolytes.[5−8] The intrinsic feature suggests that RMBs are safer than LIBs. However, the charge density of Mg^{2+} is much higher than that of Li^+ (120 vs 52 C mm^{-3}). Divalent Mg^{2+} ions suffer severe electrostatic interactions during migration and diffusion in the hosts, which raise more stringent demands on the cathodes.[9−11] Hence, recent progress is devoted to searching for appropriate cathodes for reversible magnesium storage.[12,13]

Polyanionic compounds with tetrahedral and polyhedral 3D network structures are promising and have received extensive focus due to the remarkable advantages of diverse species, high voltage, stable structure, and strong induction between polyanions, which allow fast ion diffusion.[14,15] Compared with phosphates, silicates exhibit a more stable and faster framework for Mg^{2+} storage and migration owing to the inherent lattice stability provided by the tight SiO_4 tetrahedra.[16−18] Particularly, olivine-structured $MgFeSiO_4$ is favored as RMBs cathode due to its environmental benignity, high theoretical capacity (310 mAh g^{-1}), and theoretical redox potential (~2.4 V vs Mg).[19] Islam et al. via molecular dynamics (MD) and density functional theory (DFT) calculations reveal that $MgFeSiO_4$ material has an Mg^{2+} diffusion coefficient of 10^{-9} cm^2 s^{-1} and a low migration activation energy of 0.6 eV, indicating advantageous Mg^{2+} intercalation kinetics in the $MgFeSiO_4$.[20] Besides, Orikasa et al. found that the ion-exchanged $MgFeSiO_4$ cathode can achieve an outstanding specific capacity of over 300 mAh g^{-1} at 6.62 mA g^{-1} at 55 °C.[19] However, $MgFeSiO_4$ material is confronted with low intrinsic conductivity and lacks the 1D diffusion channels for Mg^{2+} ions, which causes inferior actual test capacity.[10,15] As a result, more studies should concentrate on increasing the ion

Received: October 8, 2024
Revised: December 26, 2024
Accepted: December 31, 2024

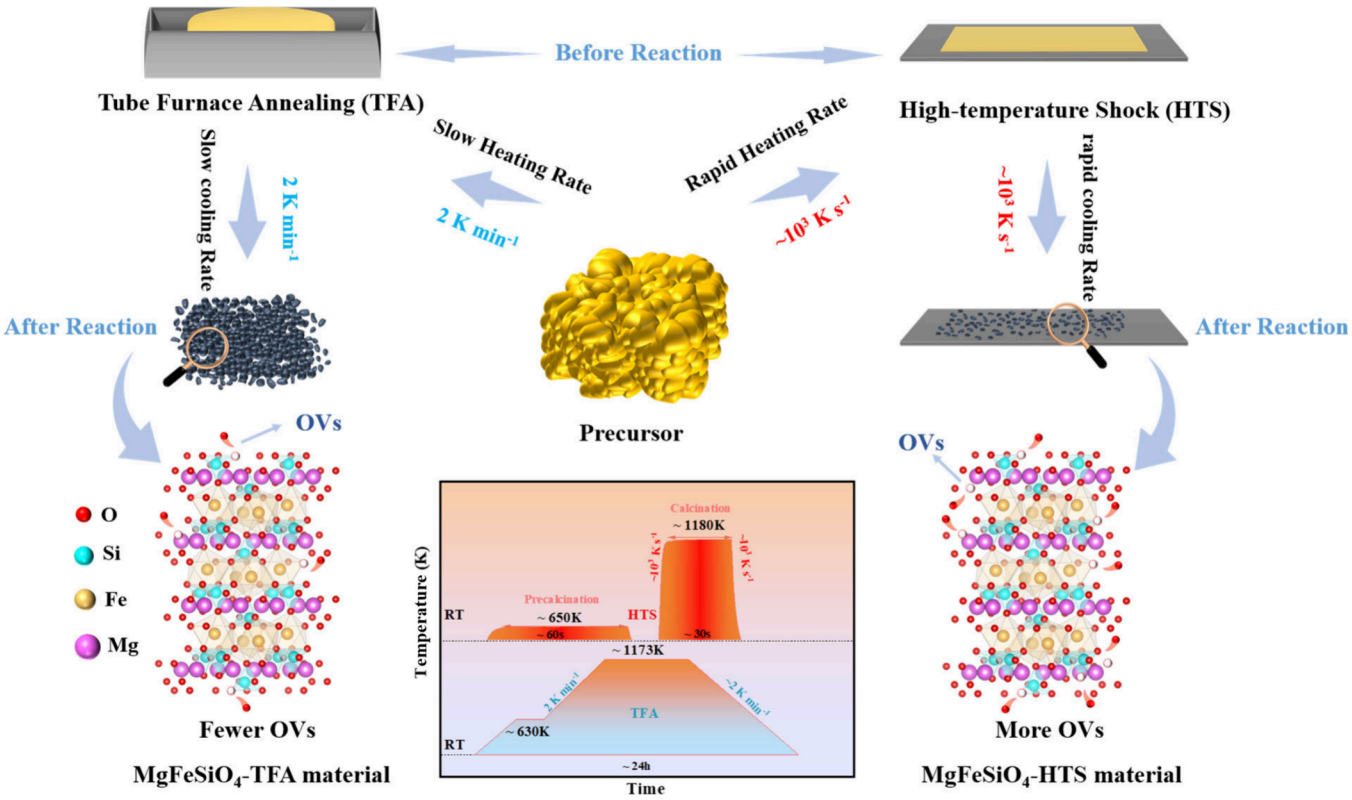

Figure 1. Schematic illustration of the formation process of $MgFeSiO_4$-HTS and the $MgFeSiO_4$-TFA material.

mobility while decreasing the Mg^{2+} diffusion and migration barriers in $MgFeSiO_4$.

Numerous methods have been proposed to promote the diffusion kinetics of cathode materials, such as constructing nanocrystalline structures,[16,18] introducing carbonaceous materials,[14,21] and doping alien ions.[22] Beyond these strategies, defect engineering has attracted extensive attention. Creating defects (i.e., dislocations, vacancies, and point defects) in the hosts is crucial in manipulating the properties.[23−26] In particular, introducing oxygen vacancies (OVs) into the cathodes can enhance ion diffusion kinetics and provide additional active sites to participate in redox charge storage.[27] Bai et al. proved that the diffusion coefficient of Zn^{2+} can be elevated 2 orders of magnitude (from 10^{-10} to 10^{-8} cm^{-2} s^{-1}) after OVs introduced in $Cu_3V_2O_7(OH)_2{\cdot}2H_2O$, thereby enhancing the reaction kinetics and electrochemical performance.[28] Wang et al. indicate that the Mg^{2+} conductivity in TiO_2 is dependent on the oxygen concentration. When incorporating OVs on the surface of TiO_2, the Mg^{2+} conductivity can reach up to 10^{-4} S cm^{-1}, owing to the OVs can capture the $[BH_4]^-$ anion and accelerate the Mg^{2+} fast migration on the solid/solid interface.[29] Zhu et al. discussed the OVs' formation energy in the *Pnma*-Li_2FeSiO_4 via the DFT calculation and found that it relates to the experimental conditions. Moreover, OVs play the role of n-type dopant elevating the electronic conductivity of Li_2FeSiO_4.[24] To date, research on OVs mainly focuses on traditional equilibrium heating processes, while it is more liable to generation in nonequilibrium reactions. Hence, regulating OVs in host materials during nonequilibrium processes and constructing the relationship between the capability and structure can help us further comprehend the role of OVs.

Herein, we put forward a strategy to introduce moderate OVs to the $MgFeSiO_4$ cathode ($MgFeSiO_4$-HTS) through ultrafast nonequilibrium high-temperature shock technology (HTS). The nonequilibrium process can get to the nucleation temperature in seconds within a fast heating rate (~10^3 K s^{-1}).[30−33] As a result, a number of OVs are produced and retained in the following short-run calcination and quenching process. In comparison, $MgFeSiO_4$ prepared in the conventional tube furnace annealing ($MgFeSiO_4$-TFA) exhibits fewer defects and the whole process is in equilibrium, along with a slow heating/cooling process (2 K min^{-1}) and long-term calcination (Figure 1). We find that the OVs weaken the interaction and energy barrier between the Mg^{2+} and $MgFeSiO_4$-HTS cathode, accelerating the Mg^{2+} diffusion kinetics. Furthermore, the as-obtained $MgFeSiO_4$-HTS cathode shows remarkable cycling properties with a reversible capacity of 85.65 and 54.43 mAh g^{-1} after 500 and 1600 cycles at 2 and 5 C, respectively, exceeding the silicate-based RMBs cathodes previously reported. This work can provide a new idea for preparing polyanionic compounds to expand their application in advanced RMBs.

To clarify the crystal phase of the obtained $MgFeSiO_4$-HTS and $MgFeSiO_4$-TFA cathodes, we utilized X-ray diffraction (XRD) measurements to investigate the crystal structures. The results shown in Figure S1a display that the diffraction peaks are well consistent with the standard structure indexed by PDF#76-0853 with no impurities.[17] Furthermore, the specific structural information is obtained through the Rietveld refinement method, and the refinement details are demonstrated in Figure S1b, S1c, and Table S1. The results illustrate that both $MgFeSiO_4$ materials have an orthorhombic structure with a space group of *Pbnm (62)*. For $MgFeSiO_4$-HTS, the refined lattice parameters are a = 4.783 Å, b = 10.309 Å, c =

https://doi.org/10.1021/acs.nanolett.4c04908
Nano Lett. XXXX, XXX, XXX−XXX

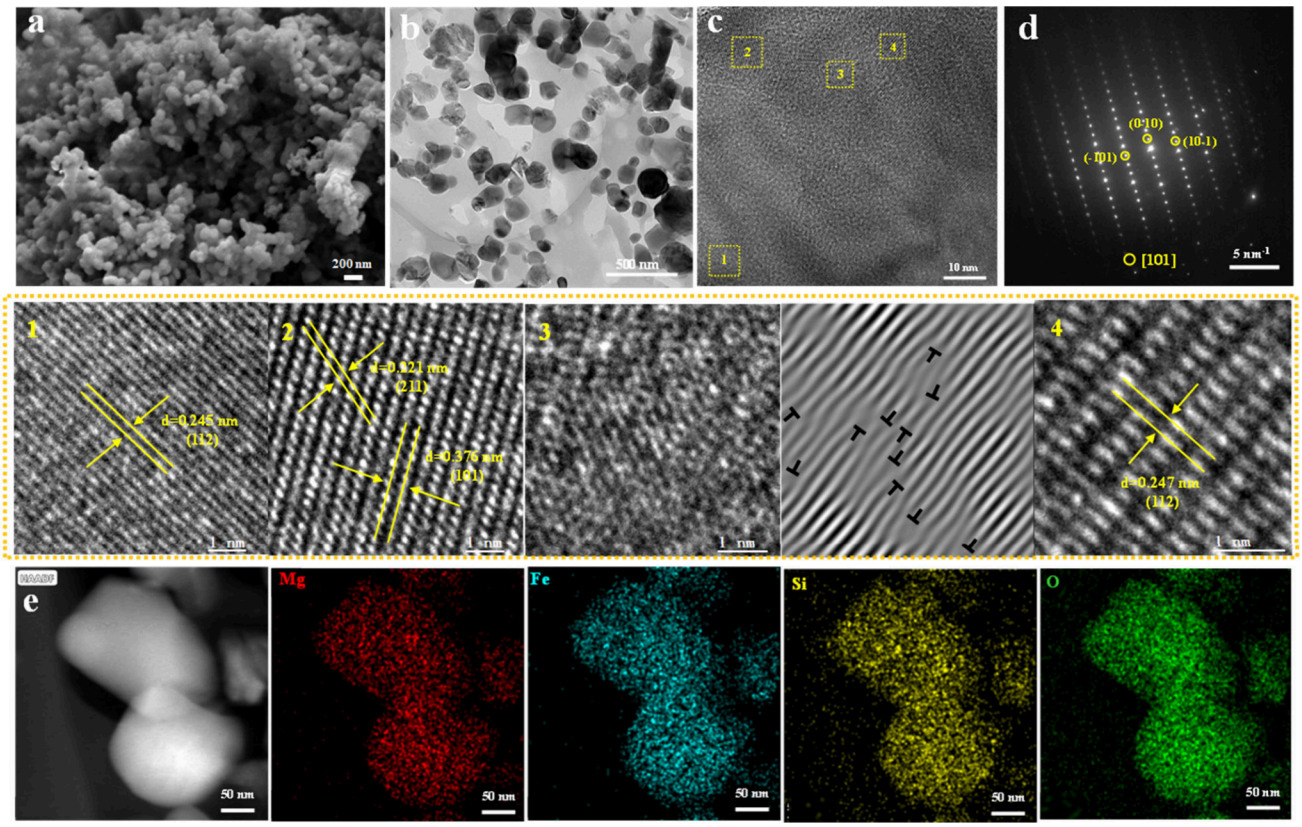

Figure 2. Structural characterization of the $MgFeSiO_4$-HTS. (a) SEM; (b) TEM; (c) HRTEM; (d) SAED patterns; (e) HADDF image and elemental mapping.

6.026 Å, and V = 297.1 Å^3, which are slightly different from those of the $MgFeSiO_4$-TFA (a = 4.795 Å, b = 10.338 Å, c = 6.041 Å, and V = 299.5 Å^3). Subsequently, scanning electron microscopy (SEM) images indicate that the $MgFeSiO_4$-HTS and $MgFeSiO_4$-TFA cathodes exhibit a similar granular micromorphology (Figure 2a, S2a). Combined with the transmission electron microscope (TEM) image in Figure 2b, the $MgFeSiO_4$-HTS has a range of 200−300 nm random shape particles. By contrast, the size of the $MgFeSiO_4$-TFA material is 300−500 nm (Figure S2b). The relatively small grain sizes of the $MgFeSiO_4$-HTS cathode can be attributed to the nonequilibrium process enabling the atoms in the precursor to migrate rapidly and the ultrashorter heating/quenching times availably suppress the particle growth.[34−36] As revealed in high-resolution TEM (HRTEM) images (Figure 2c), three sets of lattice fringes of 0.245, 0.221, and 0.376 nm in the $MgFeSiO_4$-HTS particles are matched well with (112), (211), and (101) crystal plane (Figure 2c1, 2c2, and 2c4).[17] Besides, a number of dislocations exist in $MgFeSiO_4$-HTS via the inverse fast Fourier transform (IFFT) image (Figure 2c3), which is signed with "T". And Figure 2d presents that the diffraction spot is in good agreement with the atomic arrangement of $MgFeSiO_4$-HTS with the space group along the [101] direction. As to $MgFeSiO_4$-TFA material, the lattice spacing of 0.253, 0.215, and 0.249 nm can well correspond to the interplanar distance of (131), (211), and (112) (Figure S2c1, S2c3, and S2c4). And the diffraction spot fine matches the space group along the [310] direction (Figure S 2d). Moreover, elemental mapping images indicate that Mg, Fe, Si, and O elements in $MgFeSiO_4$-HTS and $MgFeSiO_4$-TFA are uniformly dispersed, suggesting that both materials are pure phases (Figure 2e, S2e). To accurately understand the differences in specific surface area and the porosity characteristics between $MgFeSiO_4$-HTS and $MgFeSiO_4$-TFA, Brunauer−Emmett−Teller (BET) measurements are conducted (Figure S3). It can be observed that $MgFeSiO_4$-HTS has a specific surface area of 12.59 m^2 g^{-1}, along with a pore size of 35.74 nm and a pore volume of 0.12 cm^3 g^{-1}. Such mesoporous structure can facilitate fast Mg^{2+} diffusion, resulting in remarkable cycling performance.[35] The $MgFeSiO_4$-TFA possesses a mesoporous structure similar to that of $MgFeSiO_4$-HTS.

The corresponding X-ray photoelectron spectroscopy (XPS) spectra are further used to demonstrate the chemical composition of the prepared $MgFeSiO_4$-HTS and $MgFeSiO_4$-TFA materials (Figure S4a, S4b). In the $MgFeSiO_4$-HTS material, the XPS spectra for Fe 2p show that the Fe 2p peaks can be separated into Fe 2p3/2 at around 710.80 eV and Fe 2p1/2 at around 724.20 eV accompanied by the corresponding satellite peaks at around 714.76 and 728.56 eV, respectively (Figure S4c).[37−39] Similarly, the Fe 2p peaks with bonding energies of 710.51 and 724.09 eV in the $MgFeSiO_4$-TFA can correspond to Fe 2p3/2 and Fe 2p1/2, with satellite peaks at 724.09 and 728.84 eV (Figure S 4d).[40] The results suggest that the Fe valence is +2 in both $MgFeSiO_4$ cathodes, further proving that the as-prepared materials are pure phases, which can be well matched with XRD results. As shown in Figure 3a, the three peaks with bonding energies of 531.03, 531.84, and 533.13 eV in the O 1s spectra of the $MgFeSiO_4$-HTS cathode, assigned to metal oxides, oxygen vacancies (OVs), and surface-adsorbed oxygen (Os), respectively.[41,42] For the $MgFeSiO_4$-TFA cathode, the corresponding peaks of the O 1s spectrum

https://doi.org/10.1021/acs.nanolett.4c04908
Nano Lett. XXXX, XXX, XXX−XXX

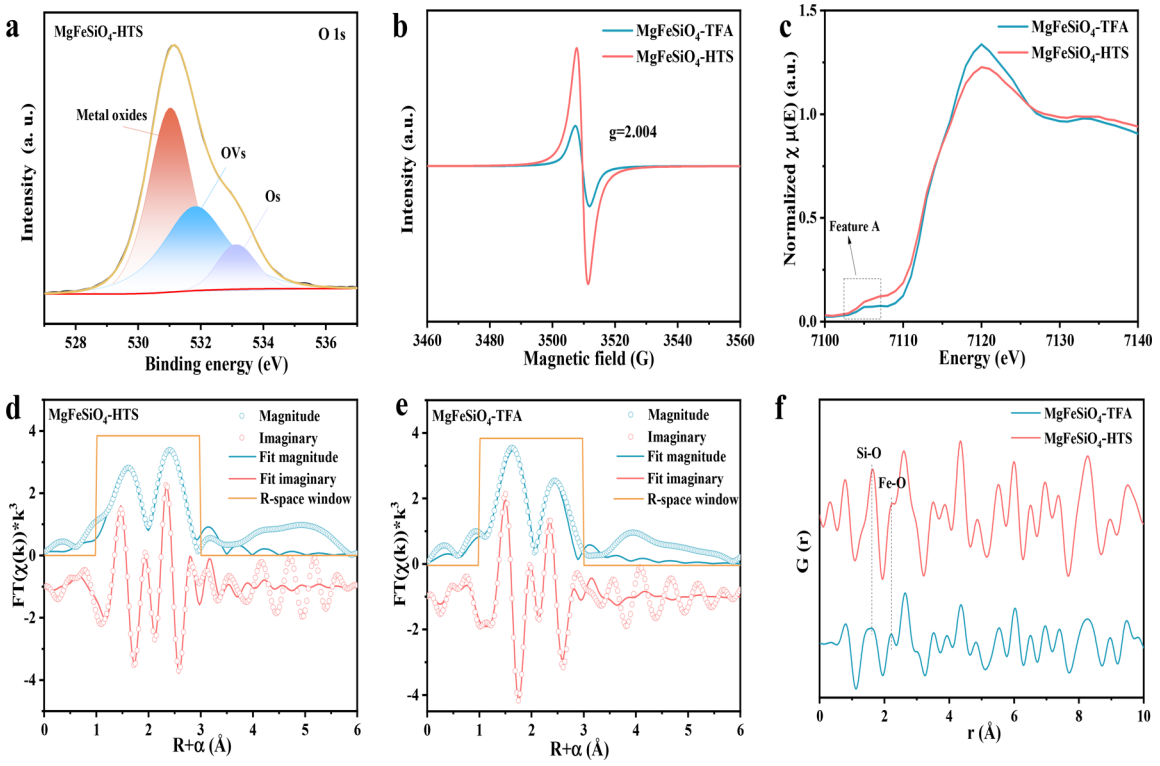

Figure 3. Structural characterization of the $MgFeSiO_4$ materials. (a) O 1s XPS spectra of $MgFeSiO_4$-HTS; (b) EPR curves; (c) Normalized Fe K-edge XANES spectra of $MgFeSiO_4$-HTS and $MgFeSiO_4$-TFA; (d) Fe K-edge EXAFS (points) and curve fit (line) for $MgFeSiO_4$-HTS, shown in R-space (FT magnitude and imaginary component). The data are k^3-weighted and not phase-corrected; (e) Fe K-edge EXAFS (points) and curve fit (line) for $MgFeSiO_4$-TFA, shown in R-space (FT magnitude and imaginary component). The data are k^3-weighted and not phase-corrected; (f) PDF spectra with peaks corresponding to interatomic distances of Si−O and Fe−O are highlighted with dashed lines.

are located at 530.76, 531.39, and 532.83 eV (Figure S4e). Meanwhile, the OVs' contents in $MgFeSiO_4$-HTS and $MgFeSiO_4$-TFA are 37.5% and 20.1%, respectively. Additionally, electron paramagnetic resonance (EPR) spectroscopy is an effective way to reveal the existence of OVs.[28] As shown in Figure 3b, $MgFeSiO_4$-TFA indicates a weak signal at g = 2.004 (a representative signal for OVs), while $MgFeSiO_4$-HTS has an intense symmetry peak. The data suggest that the ultrafast nonequilibrium reaction can contribute to generating and reserving the OVs. Analyzing the Si 2p and Mg 1s high-resolution spectrum of the $MgFeSiO_4$-HTS and $MgFeSiO_4$-TFA, they reveal similar characteristic peaks, respectively (Figure S 4f-S4i).[43,44] For better comprehension of the local structures of both $MgFeSiO_4$ materials, the X-ray absorption spectroscopy (XAS) measurements of Fe atoms are collected through X-ray absorption near-edge spectroscopy (XANES) and extended X-ray absorption fine structure (EXAFS). The similar peaks of $MgFeSiO_4$-HTS and $MgFeSiO_4$-TFA in Figure 3c suggest an analogous Fe oxidation state in both materials. Meanwhile, the pre-edge is present at feature A because of a 1s to 3d electron transition.[45] The high pre-edge features intensity of the $MgFeSiO_4$-HTS reveals a larger deviation from centrosymmetric distortion around Fe.[46] Moreover, the Fourier transformation of EXAFS spectra further identifies the bond length and coordination number in $MgFeSiO_4$-HTS and $MgFeSiO_4$-TFA (Figure 3d, 3e). The structural information derived from the EXAFS curve fitting is listed in detail in Table S2. Notably, the coordination shells of $MgFeSiO_4$-HTS and $MgFeSiO_4$-TFA can be matched well with Fe−O and Fe−Si bonds.[47,48] Qualitatively, the relatively low intensity of the first main peak in $MgFeSiO_4$-HTS can be related to the comparatively lower crystallinity or the increase of OVs. According to the given, it can be known that the shorter distance between the absorber and the two nearest-neighbor atoms in $MgFeSiO_4$-HTS is consistent with the crystal structure obtained from the XRD pattern.[49,50] Furthermore, the pair distribution function (PDF) measurement is performed to gain insight into the local structuring of Si, Fe, O, and Mg atoms (Figure 3f). For the $MgFeSiO_4$-HTS cathode, the peaks are centered at 1.62 corresponding to the Si−O pair and 2.21 for the Fe−O atomic pair, separately. And similar peaks are located at 1.60 and 2.20 Å in the $MgFeSiO_4$-TFA.[51,52] Figure S5a indicates the Raman spectra to explore the surface information on both $MgFeSiO_4$ materials, where the range from 400 to 700 cm^{-1} belongs to the Fe−O vibrations while those in the 800−1000 cm^{-1} are owing to symmetrically stretched SiO_4 vibration.[53,54] Moreover, Fourier transform infrared spectroscopy (FTIR) also explains the similar surface structural features to the above Raman results (Figure S5b).[55,56]

The electrochemical behaviors of $MgFeSiO_4$-HTS and $MgFeSiO_4$-TFA are determined to interpret the role of OVs. The cyclic voltammetry (CV) curves of both cathodes are demonstrated to research the electrochemical reaction process at a scan rate of 0.1 mV s^{-1} in Figure 4a and S6a. During the initial discharge cycle, the $MgFeSiO_4$-HTS and $MgFeSiO_4$-TFA cathodes exhibit strong cathodic peaks at 0.75 and 0.82 V, respectively, revealing irreversible solid electrolyte interphase generation and irreversible insertion of Mg^{2+} into the cathodes. In the following cycling processes, the reduction peaks are stabilized at about 1.0 V, illustrating the insertion of Mg^{2+} and the reduction of Fe^{3+} to Fe^{2+} in both cathodes. Correspond-

https://doi.org/10.1021/acs.nanolett.4c04908
Nano Lett. XXXX, XXX, XXX−XXX

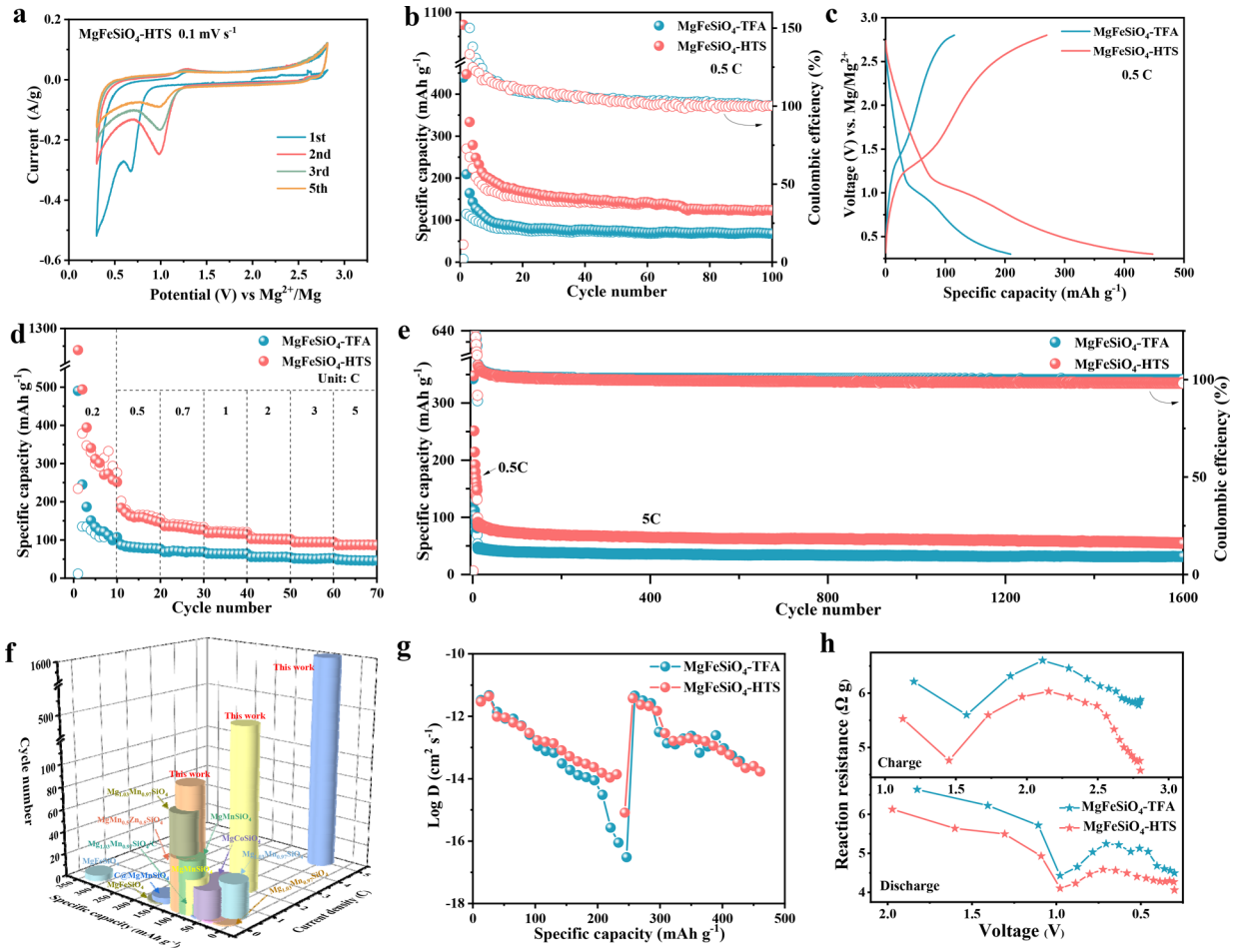

Figure 4. Electrochemical performance of $MgFeSiO_4$-HTS and $MgFeSiO_4$-TFA. (a) CV at the scan rate of 0.1 mV s^{-1} of $MgFeSiO_4$-HTS; (b) Cycling performance at 0.5 C; (c) 2nd charging/discharging profiles at 0.5 C; (d) Rate performance at various current densities of 0.2, 0.5, 1, 2, 3, and 5 C; (e) Cycling performance at 5 C; (f) Comparison in cycling performance of $MgFeSiO_4$-HTS with other reported silicate-based RMBs cathodes; (g) The Mg^{2+} diffusion coefficient and (h) reaction resistance of the $MgFeSiO_4$-HTS and $MgFeSiO_4$-TFA cathodes via the GITT technique during magnesiation and demagnesiation processes.

ingly, the $MgFeSiO_4$-HTS and $MgFeSiO_4$-TFA have a weak anodic peak recorded at 1.25 V, associating with the Fe^{2+} oxidation and the Mg^{2+} extraction.[17] Figure 4b shows the cycling performance of the $MgFeSiO_4$-TFA and $MgFeSiO_4$-HTS cathodes at a current density of 0.5 C (1 C = 156 mA g^{-1}). It can be seen that the $MgFeSiO_4$-HTS cathode has a reversible capacity of 123.93 mAh g^{-1} over 100 cycles with a Coulombic efficiency (CE) of ∼100.0%, while the specific capacity of the $MgFeSiO_4$-TFA cathode is 68.31 mAh g^{-1}. The decrease in specific capacity at the initial stage can be ascribed to optimization of the interface between the electrolyte and electrode material.[57,58] Simultaneously, according to the comparison of the second galvanostatic charge−discharge (GCD) profiles at 0.5 C (Figure 4c), the $MgFeSiO_4$-HTS and $MgFeSiO_4$-TFA respectively show a specific capacity of 447.35 and 209.25 mAh g^{-1} and reveal a similar charge and discharge platform at around 1.3 and 1.1 V. The rate performances are recorded at different current densities from 0.2 to 5 C. As expected, the $MgFeSiO_4$-HTS cathode has an outperform rate capability owing to the rich OVs. And the $MgFeSiO_4$-HTS can achieve the specific capacities of 494.1, 172.4, 135.7, 118.4, 102.7, 94.1, and 86.7 mAh g^{-1} at 0.2, 0.5, 0.7, 1, 2, 3, and 5 C. As a comparison, the $MgFeSiO_4$-TFA cathode shows the discharge-specific capacities of 244.9, 84.5, 70.3, 64.2, 55.7, 51.5, and 48.1 mAh g^{-1} (Figure 4d, S6b and S6c). Besides, Figure S6d and Figure 4e disclose the long-term cycling stability of the $MgFeSiO_4$-HTS and $MgFeSiO_4$-TFA at 2 and 5 C. Impressively, the reversible capacity of $MgFeSiO_4$-HTS is 85.7 mAh g^{-1} after 500 cycles at 2 C and even can be maintained at 54.4 mAh g^{-1} under 5 C over 1600 cycles. By contrast, the $MgFeSiO_4$-TFA cathode has a lower reversible capacity (43.8 mAh g^{-1} after 500 cycles at 2 C and 31.4 mAh g^{-1} after 1600 cycles at 5 C). These results indicate that the introduction of OVs enables improvement in the reversible kinetics of Mg^{2+} insertion and extraction, leading to a superior electrochemical performance. Moreover, the $MgFeSiO_4$-HTS also shows ascendant cycling stability and rate capability than those of other previously reported silicate polyanionic compound materials cathodes in RMBs (Figure 4f, S6e).[29,31,35,42]

To explore the nature of the outstanding rate capability and long cycling lifespan in $MgFeSiO_4$-HTS materials, the electrochemical kinetic analysis is conducted based on the CV tests under various sweeping rates from 0.1 to 1.0 mV s^{-1} (Figure S7a). Notably, the curves have analogous shapes as the scanning rate increases, manifesting good reversibility of the $MgFeSiO_4$-HTS materials.[59,60] Similar phenomena are observed in the CV testing with different scanning rates for

https://doi.org/10.1021/acs.nanolett.4c04908
Nano Lett. XXXX, XXX, XXX−XXX

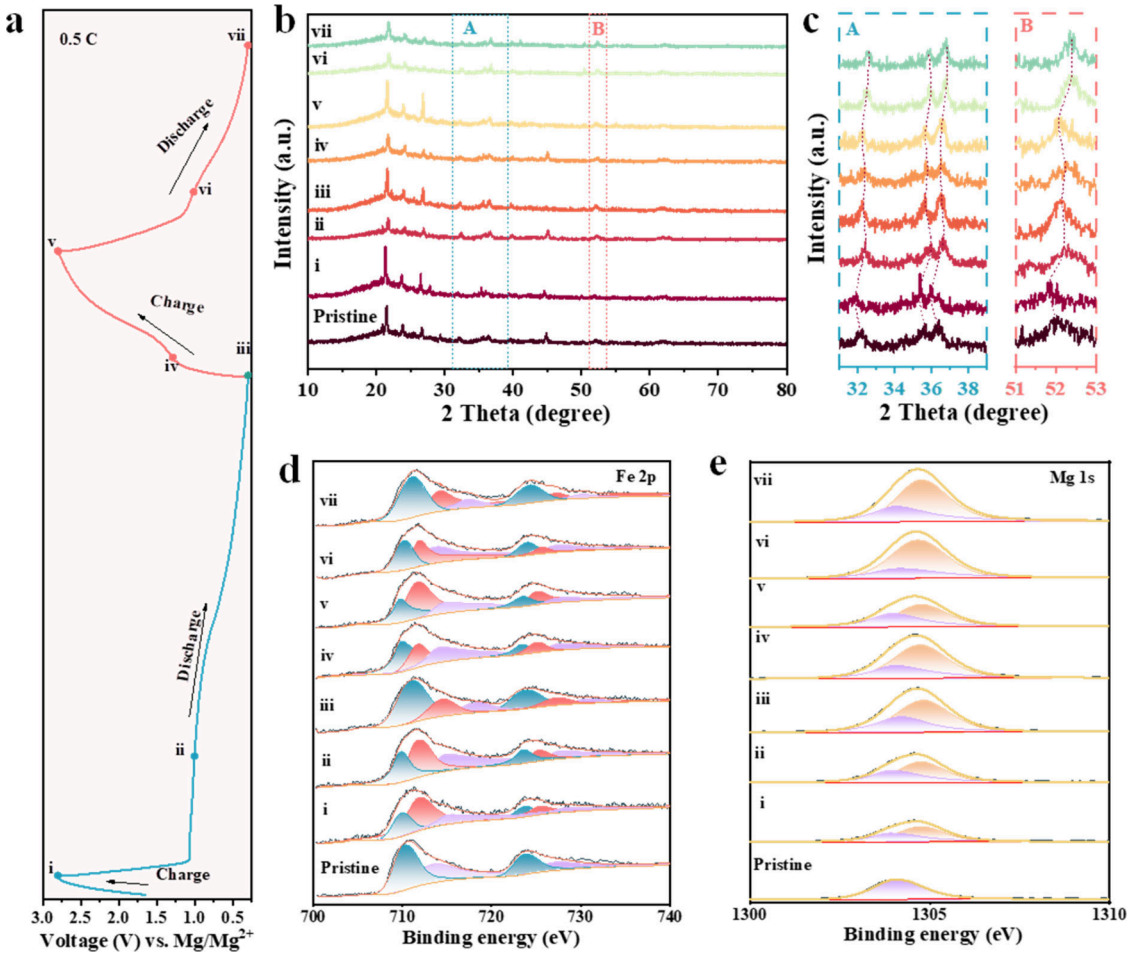

Figure 5. Magnesiation/demagnesiation mechanism and structure characterizations. (a) The discharge/charge profiles of the $MgFeSiO_4$-HTS cathode at different discharge and charge states; (b) *Ex situ* XRD patterns at different discharge and charge states; (c) Partially enlarged *ex situ* XRD patterns of (130), (131), (112), and (222) peaks at different discharge and charge states; High-resolution *ex-situ* XPS spectra of $MgFeSiO_4$-HTS: high-resolution spectra of (d) Fe 2p and (e) Mg 1s.

$MgFeSiO_4$-TFA (Figure S7b). Then the b-values are calculated according to eqs 1 and 2 to probe the contribution of capacitance-controlled and diffusion capacities. As computed in Figure S7c and S7d, the b-values of the two redox peaks for $MgFeSiO_4$-HTS are 0.61 and 0.86, while for $MgFeSiO_4$-TFA are 0.57 and 0.67. It indicates that the pseudocapacitive effect dominates the Mg^{2+} storage mechanisms of both $MgFeSiO_4$ materials.[61,62] Meanwhile, it further certifies that the capacitance contribution of both cathodes calculated via eq 3 is greater than the diffusion contribution along with increasing the sweep rates (Figure S7e, S7f). Promisingly, the pseudocapacitive contribution ratios of $MgFeSiO_4$-HTS (54%, 67%, 72%, 76%, and 79% at 0.1, 0.3, 0.5, 0.7, and 1.0 mV s^{-1}, respectively) outperform $MgFeSiO_4$-TFA (44%, 64%, 67%, 69%, and 72%, respectively). This is mainly attributed to the abundant OVs can offer more active sites and improve reaction kinetics, thereby being conducive to facilitating the electrochemical property for Mg^{2+} storage.[29,42] Then, electrochemical impedance (EIS) is adopted to understand the reaction kinetic variation and conductivity of the materials at the 30th cycle (Figure S8a). It concludes that the $MgFeSiO_4$-HTS holds lower charge-transfer resistance than $MgFeSiO_4$-TFA, identifying the faster Mg^{2+} diffusion kinetics and more efficient charge transfer in the $MgFeSiO_4$-HTS cathode.[63] Meanwhile, the Mg^{2+} diffusion coefficient (D_{Mg}^{2+}) of the $MgFeSiO_4$-HTS calculated based on eq 4 and eq 5 is 1.13×10^{-14} cm^2 s^{-1}, which is 2 orders of magnitude higher than that of $MgFeSiO_4$-TFA (8.35×10^{-16} cm^2 s^{-1}) (Figure S8b). This result confirms that the OVs are conducive to elevating the electronic conductivity and charge diffusivity. The galvanostatic intermittent titration (GITT) testing is performed to further affirm the charge transport dynamics of the electrodes during cycling (Figure S9). Figure 4g and Figure 4h illustrate the calculated D_{Mg}^{2+} and corresponding reaction resistances of $MgFeSiO_4$-HTS and $MgFeSiO_4$-TFA during the cycling. Remarkably, the D_{Mg}^{2+} values (10^{-11} - 10^{-15} cm^2 s^{-1}) for the $MgFeSiO_4$-HTS are larger than $MgFeSiO_4$-TFA (10^{-11} - 10^{-16} cm^2 s^{-1}), and the reaction resistances for the $MgFeSiO_4$-HTS are less than $MgFeSiO_4$-TFA, indicating that the OVs enable a decrease in the energy barrier of Mg^{2+} and prompt diffusion kinetics.[35,61,64,65]

To clarify the Mg^{2+} storage mechanism of the $MgFeSiO_4$-HTS material as a cathode in RMBs, *ex situ* XRD and *ex situ* XPS spectra characterizations are carried out at selected charging/discharging states in the initial and second cycles (Figure 5a). As shown in Figure 5b and 5c, the sets of peaks at ~32.2°, ~35.6°, ~36.4°, and ~52.0° are well-corresponded to (130), (131), (112), and (222) plane, respectively.[17] When first charging to 2.8 V (from pristine to i state), the mainly strong peaks slightly shift to a lower angle because of the Mg^{2+}

https://doi.org/10.1021/acs.nanolett.4c04908
Nano Lett. XXXX, XXX, XXX−XXX

extraction.[59] Then, these peaks are moved to a higher angle as discharge from i to iii state, which may be due to the inserted Mg^{2+} ions coordinating with the lattice oxygen, causing the layer spacing reduction.[66] Notably, a phenomenon similar to that presented above also occurs in the second cycling (from the iv to vii state). Simultaneously, only the shift of peak positions appeared without the new peak presence during the cycling, verifying no new phase generation.[67] Besides, the peaks located at ~21.4°, ~24.1°, and ~26.7° are well-matched to the precipitated $MgCl_2$ (JCPDS card no. 01-070-2746) and the conductive agent (JCPDS card no. 00-026-1076), respectively.[66] In addition, *ex situ* XPS spectra of Fe 2p and Mg 1s at various charge−discharge depths are shown in Figure 5d and 5e. As charging up to i state, the Fe 2p spectrum of the $MgFeSiO_4$-HTS can be separated into three peaks at around 709.86, 711.79, and 723.66 eV, corresponding to Fe^{2+}, Fe^{3+}, and their satellite peaks.[37] In this stage, the Fe^{3+}/ Fe^{2+} ratio is 1.83, showing that Fe^{3+} is the dominant oxidation state of iron, accompanied by Mg^{2+} extraction. When discharged to state ii and further to state iii, the Fe^{3+} signals are gradually weak, while the Fe^{2+} peaks are distinctly intensified. Meanwhile, the Fe^{3+}/ Fe^{2+} ratio progressively decreases to 0.93 and 0.42, illustrating the charge transfer during the Mg^{2+} insertion process. As expected, the Fe 2p spectra also follow the given change pattern in the second charge (iv and v states) and discharge (vi and vii states) process. From the Mg 1s spectrum of the $MgFeSiO_4$-HTS cathode at various cutoff voltage states (Figure 5e), only a Mg 1s signal emerges at 1303.9 eV for the pristine material, implying only Mg^{2+} existence before cycling. Interestingly, the Mg 1s spectrum in the cycling processes can be deconvoluted into another peak centered at 1304.7 eV, which can be well-matched with $MgCl^+$.[68] Therefore, it demonstrates a cointercalation/extraction behavior of Mg^{2+} and $MgCl^+$ in the $MgFeSiO_4$-HTS during the repetitive cycling.[59]

The superbly elevated Mg^{2+} diffusion kinetics and electrochemical performance of the $MgFeSiO_4$-HTS, compared with conventional $MgFeSiO_4$-TFA, are noticed to be closely associated with the OVs. Then, DFT calculations are employed to analyze the diffusion process in the $MgFeSiO_4$-HTS and $MgFeSiO_4$-TFA cathodes based on the OVs as variables. Figure S10 shows the OVs structure schematic diagrams of both of the $MgFeSiO_4$ materials. As Figure S11a and S11b explained, the projected density of states (PDOS) values at the Fermi level of $MgFeSiO_4$-TFA and $MgFeSiO_4$-HTS are 30.76 and 35.72 eV, respectively, indicating the higher electronic conductivity in $MgFeSiO_4$-HTS.[42] To verify the effect of OVs on the diffusion of Mg^{2+} and $MgCl^+$ in $MgFeSiO_4$-TFA and $MgFeSiO_4$-HTS, the corresponding adsorption models are displayed in Figure S12. According to Figure S13, it can be found that the total adsorption energy of $Mg^{2+}/MgCl^+$ in $MgFeSiO_4$-HTS is lower than that in $MgFeSiO_4$-TFA, declaring a weaker interaction between the $Mg^{2+}/MgCl^+$ and the $MgFeSiO_4$-HTS. Subsequently, the calculated diffusion energy barriers and the corresponding diffusion paths of $Mg^{2+}/MgCl^+$ in $MgFeSiO_4$-TFA and $MgFeSiO_4$-HTS are disclosed in Figure S14−S16. As expected, the $MgFeSiO_4$-TFA has a higher $Mg^{2+}/MgCl^+$ diffusion energy barrier than $MgFeSiO_4$-HTS, revealing that due to the abundant OVs in $MgFeSiO_4$-HTS, it has an electrostatic repulsion against the inserted ions, thereby weakening the electrostatic interactions between ions and the $MgFeSiO_4$-HTS electrode.[59,63] Consequently, when OVs exist in the material, the diffusion kinetics of Mg^{2+} can be efficiently facilitated to achieve diffusion regulation, further enhancing the electrochemical performance.

In summary, the appropriate number of OVs has been successfully introduced into the olivine-type $MgFeSiO_4$-HTS cathode via the ultrafast nonequilibrium HTS technique. The product shows an electrochemical property higher than that prepared by the conventional sintering method. Impressively, the $MgFeSiO_4$-HTS displays a reversible capacity of 85.65 and 54.43 mAh g^{-1} after 500 and 1600 cycles at 2 and 5 C, respectively. By integration of experimental evidence and kinetic analysis, it can be concluded that the OVs effectively weaken the interaction and energy barrier between the Mg^{2+} ions and the $MgFeSiO_4$-HTS cathode. In addition, the $MgFeSiO_4$-HTS cathode indicates superb electrochemical properties and long-term cycling lifespans compared to other silicate-based RMBs cathodes previously reported.

■ ASSOCIATED CONTENT

Supporting Information

The Supporting Information is available free of charge at https://pubs.acs.org/doi/10.1021/acs.nanolett.4c04908.

Additional details of sample preparation, material characterization, electrochemical measurements, and simulations; material characterization graphs (XRD, SEM, TEM, EDS, BET, XPS, Raman, and FTIR); and electrochemical performance graphs (CV, rate charge−discharge curve, cycling performances, comparison of rate performance between this work and the reported cathodes, CV profiles at various scan rates and the linear fitting for determining b values, the pseudocapacitive and diffusion contributions of this work at different scan rates, and EIS profiles) (PDF)

■ AUTHOR INFORMATION

Corresponding Authors

Guangsheng Huang − *National Innovation Center for Industry-Education Integration of Energy Storage Technology, College of Materials Science and Engineering, Chongqing University, Chongqing 400044, China; Chongqing Institute of New Energy Storage Materials and Equipment, Chongqing 401122, China;* orcid.org/0000-0002-7379-6893; Email: gshuang@cqu.edu.cn

Yanan Chen − *School of Materials Science and Engineering, Key Laboratory of Advanced Ceramics and Machining Technology of Ministry of Education, Tianjin Key Laboratory of Composite and Functional Materials, Tianjin University, Tianjin 300072, China;* orcid.org/0000-0002-6346-6372; Email: yananchen@tju.edu.cn

Jili Yue − *National Innovation Center for Industry-Education Integration of Energy Storage Technology, College of Materials Science and Engineering, Chongqing University, Chongqing 400044, China; Chongqing Institute of New Energy Storage Materials and Equipment, Chongqing 401122, China;* orcid.org/0009-0000-5425-2260; Email: jili.yue@cqu.edu.cn

Authors

Jie Xu − *National Innovation Center for Industry-Education Integration of Energy Storage Technology, College of Materials Science and Engineering, Chongqing University, Chongqing 400044, China; Chongqing Institute of New Energy Storage Materials and Equipment, Chongqing*

https://doi.org/10.1021/acs.nanolett.4c04908
Nano Lett. XXXX, XXX, XXX−XXX

401122, China; School of Materials Science and Engineering, Key Laboratory of Advanced Ceramics and Machining Technology of Ministry of Education, Tianjin Key Laboratory of Composite and Functional Materials, Tianjin University, Tianjin 300072, China

Yuqi Hong − *National Innovation Center for Industry-Education Integration of Energy Storage Technology, College of Materials Science and Engineering, Chongqing University, Chongqing 400044, China; Chongqing Institute of New Energy Storage Materials and Equipment, Chongqing 401122, China*

Shuming Dou − *School of Materials Science and Engineering, Key Laboratory of Advanced Ceramics and Machining Technology of Ministry of Education, Tianjin Key Laboratory of Composite and Functional Materials, Tianjin University, Tianjin 300072, China*

Junhan Wu − *National Innovation Center for Industry-Education Integration of Energy Storage Technology, College of Materials Science and Engineering, Chongqing University, Chongqing 400044, China; Chongqing Institute of New Energy Storage Materials and Equipment, Chongqing 401122, China*

Jingchao Zhang − *School of Materials Science and Engineering, Key Laboratory of Advanced Ceramics and Machining Technology of Ministry of Education, Tianjin Key Laboratory of Composite and Functional Materials, Tianjin University, Tianjin 300072, China*

Qingmeng Wang − *National Innovation Center for Industry-Education Integration of Energy Storage Technology, College of Materials Science and Engineering, Chongqing University, Chongqing 400044, China; Chongqing Institute of New Energy Storage Materials and Equipment, Chongqing 401122, China*

Tiantian Wen − *National Innovation Center for Industry-Education Integration of Energy Storage Technology, College of Materials Science and Engineering, Chongqing University, Chongqing 400044, China; Chongqing Institute of New Energy Storage Materials and Equipment, Chongqing 401122, China*

Yang Song − *National Innovation Center for Industry-Education Integration of Energy Storage Technology, College of Materials Science and Engineering, Chongqing University, Chongqing 400044, China; Chongqing Institute of New Energy Storage Materials and Equipment, Chongqing 401122, China*

Wei-Di Liu − *School of Chemistry and Physics, ARC Research Hub in Zero-emission Power Generation for Carbon Neutrality, and Centre for Materials Science, Queensland University of Technology, Brisbane, Queensland 4000, Australia;* orcid.org/0000-0002-8271-639X

Jianrong Zeng − *Shanghai Synchrotron Radiation Facility, Shanghai Advanced Research Institute, Chinese Academy of Sciences, Shanghai 201204, China; Shanghai Institute of Applied Physics, Chinese Academy of Sciences, Shanghai 201800, China*

Chaohe Xu − *National Innovation Center for Industry-Education Integration of Energy Storage Technology, College of Materials Science and Engineering, Chongqing University, Chongqing 400044, China; Chongqing Institute of New Energy Storage Materials and Equipment, Chongqing 401122, China;* orcid.org/0000-0002-1345-1420

Jingfeng Wang − *National Innovation Center for Industry-Education Integration of Energy Storage Technology, College of Materials Science and Engineering, Chongqing University, Chongqing 400044, China; Chongqing Institute of New Energy Storage Materials and Equipment, Chongqing 401122, China*

Fusheng Pan − *National Innovation Center for Industry-Education Integration of Energy Storage Technology, College of Materials Science and Engineering, Chongqing University, Chongqing 400044, China; Chongqing Institute of New Energy Storage Materials and Equipment, Chongqing 401122, China*

Complete contact information is available at: https://pubs.acs.org/10.1021/acs.nanolett.4c04908

Notes

The authors declare no competing financial interest.

■ ACKNOWLEDGMENTS

This work is supported by the National Key Research and Development Program (No. 2021YFB3701000); the National Natural Science Foundation of China (Nos. U2037601, 52171219, and 91963113); the Chongqing Technology Innovation and Application Development Project (No. CSTB2022TIAD-KPX0028). The authors thank the staff of beamline BL13SSW at Shanghai Synchrotron Radiation Facility for experiment support.

■ REFERENCES

(1) Shin, C.-H.; Lee, H.-Y.; Gyan-Barimah, C.; Yu, J.-H.; Yu, J.-S. Magnesium: Properties and Rich Chemistry for New Material Synthesis and Energy Applications. *Chem. Soc. Rev.* **2023**, *52* (6), 2145−2192.

(2) Liu, F.; Wang, T.; Liu, X.; Fan, L. Challenges and Recent Progress on Key Materials for Rechargeable Magnesium Batteries. *Adv. Energy Mater.* **2021**, *11* (2), No. 2000787.

(3) Sun, C.; Wang, H.; Yang, F.; Tang, A.; Huang, G.; Li, L.; Wang, Z.; Qu, B.; Xu, C.; Tan, S.; Zhou, X.; Wang, J.; Pan, F. Layered Buserite Mg-Mn Oxide Cathode for Aqueous Rechargeable Mg-Ion Battery. *J. Magnes. Alloy* **2023**, *11* (3), 840−850.

(4) Li, Y.; Zheng, Y.; Guo, K.; Zhao, J.; Li, C. Mg-Li Hybrid Batteries: The Combination of Fast Kinetics and Reduced Overpotential. *Energy Mater. Adv.* **2022**, *2022*, No. 9840837.

(5) Blázquez, J.; Maça, R.; Leonet, O.; Azaceta, E.; Mukherjee, A.; Zhao-Karger, Z.; Li, Z.; Kovalevsky, A.; Fernández-Barquín, A.; Mainar, A.; Jankowski, P.; Rademacher, L.; Dey, S.; Dutton, S.; Grey, C.; Drews, J.; Häcker, J.; Danner, T.; Latz, A.; Sotta, D.; Palacin, M.; Martin, J.; Lastra, J.; Fichtner, M.; Kundu, S.; Kraytsberg, A.; Yair, E.; Noked, M.; Aurbach, D. A Practical Perspective on the Potential of Rechargeable Mg Batteries. *Energy Environ. Sci.* **2023**, *16* (5), 1964−1981.

(6) Tan, S.; Xu, J.; Deng, R.; Zhao, Q.; Xu, C.; Huang, G.; Wang, J.; Pan, F. A Perspective on the Key Factors of Safety for Rechargeable Magnesium Batteries. *J. Energy Chem.* **2024**, *94*, 656−676.

(7) Zhou, L.; Shen, C.; Hou, X.; Fang, Z.; Jin, T.; Xie, K. Re-Delocalization of Localized *d*-Electrons in VO_2(R)-VS_4 Hetero-Structure Enables High Performance of Rechargeable Mg-Ion Batteries. *J. Magnes. Alloy* **2024**, *12* (5), 1830−1840.

(8) Ralls, A. M.; Daroonparvar, M.; Menezes, P. L. Spark Plasma Sintering of Mg-Based Alloys: Microstructure, Mechanical Properties, Corrosion Behavior, and Tribological Performance. *J. Magnes. Alloy* **2024**, *12* (2), 405−442.

(9) Bonnick, P.; Muldoon, J. A Trip to Oz and a Peak Behind the Curtain of Magnesium Batteries. *Adv. Funct. Mater.* **2020**, *30* (21), No. 1910510.

(10) Li, Z.; Han, L.; Wang, Y.; Li, X.; Lu, J.; Hu, X. Microstructure Characteristics of Cathode Materials for Rechargeable Magnesium Batteries. *Small* **2019**, *15* (32), No. 1900105.

(11) Li, M.; Lu, J.; Ji, X. l.; Li, Y.; Shao, Y.; Chen, Z.; Zhong, C.; Amine, K. Design Strategies for Nonaqueous Multivalent-Ion and Monovalent-Ion Battery Anodes. *Nat. Rev. Mater.* **2020**, *5* (4), 276−294.
(12) Zhang, Q.; Hu, Y.; Wang, J.; Pan, F. Low-Temperatures Synthesis of CuS Nanospheres as Cathode Material for Magnesium Second Batteries. *J. Magnes. Alloy* **2023**, *11* (1), 192−200.
(13) He, X.; Cheng, R.; Sun, X.; Xu, H.; Li, Z.; Sun, F.; Zhan, Y.; Zou, J.; Laine, R. M. Organic Cathode Materials for Rechargeable Magnesium-Ion Batteries: Fundamentals, Recent Advances, and Approaches to Optimization. *J. Magnes. Alloy* **2023**, *11* (12), 4359−4389.
(14) Rubio, S.; Liang, Z.; Li, Y.; Zuo, W.; Lavela, P.; Tirado, J.; Liu, R.; Zhou, K.; Zhu, J.; Zheng, B.; Liu, X.; Yang, Y.; Ortiz, G. Exploring Hybrid Mg^{2+}/H^{+} Reactions of C@$MgMnSiO_4$ with Boosted Voltage in Magnesium-Ion Batteries. *Electrochim. Acta* **2022**, *404*, No. 139738.
(15) Kotobuki, M.; Yan, B.; Lu, L. Recent Progress on Cathode Materials for Rechargeable Magnesium Batteries. *Energy Storage Mater.* **2023**, *54*, 227−253.
(16) Truong, Q.; Devaraju, M. K.; Honma, I. Nanocrystalline $MgMnSiO_4$ and $MgCoSiO_4$ Particles for Rechargeable Mg-Ion Batteries. *J. Power Sources* **2017**, *361*, 195−202.
(17) Li, Y.; Nuli, Y.; Yang, J.; Yilinuer, T.; Wang, J. $MgFeSiO_4$ Prepared via a Molten Salt Method as a New Cathode Material for Rechargeable Magnesium Batteries. *Chin. Sci. Bull.* **2011**, *56* (4−5), 386−390.
(18) Feng, Z.; Yang, J.; NuLi, Y.; Wang, J. Sol-Gel Synthesis of $Mg_{1.03}Mn_{0.97}SiO_4$ and Its Electrochemical Intercalation Behavior. *J. Power Sources* **2008**, *184* (2), 604−609.
(19) Orikasa, Y.; Masese, T.; Koyama, Y.; Mori, T.; Hattori, M.; Yamamoto, K.; Okado, T.; Huang, Z.; Minato, T.; Tassel, C.; Kim, J.; Kobayashi, Y.; Abe, T.; Kageyama, H.; Uchimoto, Y. High Energy Density Rechargeable Magnesium Battery Using Earth-Abundant and Non-Toxic Elements. *Sci. Rep.* **2014**, *4* (1), 5622.
(20) Heath, J.; Chen, H.; Islam, M. $MgFeSiO_4$ as a Potential Cathode Material for Magnesium Batteries: Ion Diffusion Rates and Voltage Trends. *J. Mater. Chem. A* **2017**, *5* (25), 13161−13167.
(21) NuLi, Y.; Zheng, Y.; Wang, F.; Yang, J.; Minett, A.; Wang, J.; Chen, J. MWNT/C/$Mg_{1.03}Mn_{0.97}SiO_4$ Hierarchical Nanostructure for Superior Reversible Magnesium Ion Storage. *Electrochem. Commun.* **2011**, *13* (10), 1143−1146.
(22) Pérez-Vicente, C.; Rubio, S.; Ruiz, R.; Zuo, W.; Liang, Z.; Yang, Y.; Ortiz, G. F. Olivine-Type $MgMn_{0.5}Zn_{0.5}SiO_4$ Cathode for Mg-Batteries: Experimental Studies and First Principles Calculations. *Small* **2023**, *19*, No. 2206010.
(23) Zhang, J.; Chang, Z.; Zhang, Z.; Du, A.; Dong, S.; Li, Z.; Li, G.; Cui, G. Current Design Strategies for Rechargeable Magnesium-Based Batteries. *ACS Nano* **2021**, *15* (10), 15594−15624.
(24) Zhang, L.; Wu, S.; Shuai, J.; Hou, Z.; Zhu, Z. Formation of Oxygen Vacancies in Li_2FeSiO_4: First-Principles Calculations. *Phys. Chem. Chem. Phys.* **2021**, *23*, 20444.
(25) Mao, F.; Guo, W.; Ma, J. Research Progress on Design Strategies, Synthesis and Performance of $LiMn_2O_4$-Based Cathodes. *RSC Adv.* **2015**, *5* (127), 105248−105258.
(26) Jiang, R.; Liu, B.; Du, C.; Jin, M.; Liu, X.; Ma, X.; Zhu, Y.; Zou, M.; Cao, C. Microwave-induced defect-rich vanadium sulfide cathodes for highly reversible electrochemical magnesium storage. *Chem. Eng. J.* **2024**, *488*, No. 150487.
(27) Zhang, Y.; Chen, P.; Wang, Q.; Wang, Q.; Zhu, K.; Ye, K.; Wang, G.; Cao, D.; Yan, J.; Zhang, Q. High-Capacity and Kinetically Accelerated Lithium Storage in MoO_3 Enabled by Oxygen Vacancies and Heterostructure. *Adv. Energy Mater.* **2021**, *11* (31), No. 2101712.
(28) Bai, Y.; Zhang, H.; Xiang, B.; Hao, J.; Yan, L.; Zhu, C. Oxygen Vacancy-Rich, Binder-Free Copper Pyrovanadate for Zinc Ion Storage. *Chem. Eng. J.* **2021**, *420*, No. 130474.
(29) Wang, Q.; Li, H.; Zhang, R.; Liu, Z.; Deng, H.; Cen, W.; Yan, Y.; Chen, Y. Oxygen Vacancies Boosted Fast Mg^{2+} Migration in Solids at Room Temperature. *Energy Storage Mater.* **2022**, *51*, 630−637.
(30) Jiang, H.; Zeng, C.; Zhu, W.; Luo, J.; Liu, Z.; Zhang, J.; Liu, R.; Xu, Y.; Chen, Y.; Hu, W. Boosting Cycling Stability by Regulating Surface Oxygen Vacancies of LNMO by Rapid Calcination. *Nano Res.* **2024**, *17* (4), 2671−2677.
(31) Zhu, W.; Zhang, J.; Luo, J.; Zeng, C.; Su, H.; Zhang, J.; Liu, R.; Hu, E.; Liu, Y.; Liu, W.; Chen, Y.; Hu, W.; Xu, Y. Ultrafast Non-Equilibrium Synthesis of Cathode Materials for Li-Ion Batteries. *Adv. Mater.* **2023**, *35* (2), No. 2208974.
(32) Guo, Z.; Jiang, H.; Sun, X.; Li, X.; Liu, Z.; Zhang, J.; Luo, J.; Zhang, J.; Tao, X.; Ding, J.; Han, X.; Liu, R.; Chen, Y.; Hu, W. Ultrafast Non-Equilibrium Phase Transition Induced Twin Boundaries of Spinel Lithium Manganate. *Adv. Energy Mater.* **2024**, *14* (5), No. 2302484.
(33) Liu, S.; Hu, Z.; Wu, Y.; Zhang, J.; Zhang, Y.; Cui, B.; Liu, C.; Hu, S.; Zhao, N.; Han, X.; Cao, A.; Chen, Y.; Deng, Y.; Hu, W. Dislocation-Strained IrNi Alloy Nanoparticles Driven by Thermal Shock for the Hydrogen Evolution Reaction. *Adv. Mater.* **2020**, *32* (48), No. 2006034.
(34) Xie, H.; Hong, M.; Hitz, E.; Wang, X.; Cui, M.; Kline, D.; Zachariah, M.; Hu, L. High-Temperature Pulse Method for Nanoparticle Redispersion. *J. Am. Chem. Soc.* **2020**, *142* (41), 17364−17371.
(35) Dou, S.; Xu, J.; Zhang, D.; Liu, W.; Zeng, C.; Zhang, J.; Liu, Z.; Wang, H.; Liu, Y.; Wang, Y.; He, Y.; Liu, W.; Gan, W.; Chen, Y.; Yuan, Q. Ultrarapid Nanomanufacturing of High-Quality Bimetallic Anode Library toward Stable Potassium-Ion Storage. *Angew. Chem., Int. Ed.* **2023**, *62* (26), No. e202303600.
(36) Dou, S.; Xu, J.; Cui, X.; Liu, W.; Zhang, Z.; Deng, Y.; Hu, W.; Chen, Y. High-Temperature Shock Enabled Nanomanufacturing for Energy-Related Applications. *Adv. Energy Mater.* **2020**, *10* (33), No. 2001331.
(37) Yamashita, T.; Hayes, P. Analysis of XPS Spectra of Fe^{2+} and Fe^{3+} Ions in Oxide Materials. *Appl. Surf. Sci.* **2008**, *254* (8), 2441−2449.
(38) Li, H.; Zhu, J.; Huang, X.; Zhou, T.; Ren, Y. Enhancing Lithium-Ion and Electric Conductive Li_2FeSiO_4 Cathode through in Situ Boron-Doping and Carbon-Coating Strategy. *Rare Met.* **2022**, *41* (12), 4055−4064.
(39) Singh, P.; Shiva, K.; Celio, H.; Goodenough, J. Eldfellite, $NaFe(SO_4)_2$: An Intercalation Cathode Host for Low-Cost Na-Ion Batteries. *Energy Environ. Sci.* **2015**, *8* (10), 3000−3005.
(40) Guan, W.; Pan, B.; Zhou, P.; Mi, J.; Zhang, D.; Xu, J.; Jiang, Y. A High Capacity, Good Safety and Low Cost Na_2FeSiO_4-Based Cathode for Rechargeable Sodium-Ion Battery. *ACS Appl. Mater. Interfaces* **2017**, *9* (27), 22369−22377.
(41) Liu, W.; Pang, Y.; Shi, Z.; Yue, H.; Dong, H.; Cao, Z.; Yang, Z.; Yang, S.; Yin, Y. Ultrafast Kinetics in a PAN/$MgFe_2O_4$ Flexible Free-Standing Anode Induced by Heterojunction and Oxygen Vacancies. *ACS Appl. Mater. Interfaces* **2022**, *14* (9), 11575−11586.
(42) Ye, J.; Li, P.; Zhang, H.; Song, Z.; Fan, T.; Zhang, W.; Tian, J.; Huang, T.; Qian, Y.; Hou, Z.; Shpigel, N.; Chen, L.; Dou, S. Manipulating Oxygen Vacancies to Spur Ion Kinetics in V_2O_5 Structures for Superior Aqueous Zinc-Ion Batteries. *Adv. Funct. Mater.* **2023**, *33* (46), No. 2305659.
(43) Yi, L.; Wang, X.; Wang, G.; Bai, Y.; Liu, M.; Wang, X.; Yu, R. Improved Electrochemical Performance of Spherical Li_2FeSiO_4/C Cathode Materials via Mn Doping for Lithium-Ion Batteries. *Electrochim. Acta* **2016**, *222*, 1354−1364.
(44) Xu, Y.; Li, Y.; Liu, S.; Li, H.; Liu, Y. Nanoparticle Li_2FeSiO_4 as Anode Material for Lithium-Ion Batteries. *J. Power Sources* **2012**, *220*, 103−107.
(45) Muthiah, A.; Baikie, T.; Shukla, S.; Ball, S.; Copley, M.; Hyde, T.; Du, Y.; Sankar, G.; Aravindan, V.; Srinivasan, M. Ex Situ XAS Investigation of Effect of Binders on Electrochemical Performance of $Li_2Fe(SO_4)_2$ Cathode. *J. Mater. Chem. A* **2017**, *5* (37), 19963−19971.
(46) Wiriya, N.; Chantrasuwan, P.; Kaewmala, S.; Nash, J.; Srilomsak, S.; Meethong, N.; Limphirat, W. Doping Effect of Manganese on the Structural and Electrochemical Properties of

https://doi.org/10.1021/acs.nanolett.4c04908
Nano Lett. XXXX, XXX, XXX−XXX

Li_2FeSiO_4 Cathode Materials for Rechargeable Li-Ion Batteries. *Radiat. Phys. Chem.* **2020**, *171*, No. 108753.
(47) Latif, C.; Firdausi, A.; Nihlatunnur, N.; Saiyasombat, C.; Klysubun, W.; Subhan, A.; Zainuri, M.; Pratapa, S. Synchrotron Crystal and Local Structures, Microstructure, and Electrical Characterization of Cu-Doped $LiFePO_4$/C via Dissolution Method with Ironstone as Fe Source. *J. Mater. Sci: Mater. Electron.* **2022**, *33* (22), 17722−17732.
(48) Brownrigg, A.; Mountjoy, G.; Chadwick, A.; Alfredsson, M.; Bras, W.; Billaud, J.; Armstrong, A.; Bruce, P.; Dominko, R.; Kelder, E. In Situ Fe K-Edge X-Ray Absorption Spectroscopy Study during Cycling of Li_2FeSiO_4 and $Li_{2.2}Fe_{0.9}SiO_4$ Li Ion Battery Materials. *J. Mater. Chem. A* **2015**, *3* (14), 7314−7322.
(49) Toyama, T.; Hirano, T.; Okumura, T.; Horiba, T. X-Ray Absorption Fine Structure Analysis for Crystal Structure Change of Vanadium-Substituted Lithium Silicate, $Li_{2.2}Fe_{0.4}Mn_{0.4}Si_{0.8}V_{0.2}O_4$, during Charge-Discharge Cycles. *J. Power Sources* **2019**, *443*, No. 227189.
(50) Fornasini, P.; Grisenti, R. On EXAFS Debye-Waller Factor and Recent Advances. *J. Synchrotron Rad.* **2015**, *22* (5), 1242−1257.
(51) Eveillard, F.; Gervillié, C.; Taviot-Guého, C.; Leroux, F.; Guérin, K.; Sougrati, M. T.; Belin, S.; Delbègue, D. Unravelling Lithiation Mechanisms of Iron Trifluoride by *Operando* X-Ray Absorption Spectroscopy and MCR-ALS Chemometric Tools. *New J. Chem.* **2020**, *44* (24), 10153−10164.
(52) Shyam, B.; Chapman, K.; Balasubramanian, M.; Klingler, R.; Srajer, G.; Chupas, P. Structural and Mechanistic Revelations on an Iron Conversion Reaction from Pair Distribution Function Analysis. *Angew. Chem., Int. Ed.* **2012**, *51* (20), 4852−4855.
(53) Zhang, Q.; Ji, S.; Yan, C.; Wang, X. Insights into the Porosity and Electrochemical Performance of Nano Li_2FeSiO_4 and Li_2FeSiO_4/C Composite Cathode Materials. *Mater. Technol.* **2022**, *37* (9), 1195−1204.
(54) Pazhaniswamy, S.; Parameswaran, A.; Balakrishnan, N.; Goel, S.; Sofer, Z.; Yadav, S.; Panneerselvam, C. Prediction Clue on the Fading Capacity of Multi-Walled Carbon Nanotube-Decorated $Li_2(Fe_{1-x}Ti_x)SiO_4$/C High-Performance Cathode Materials. *Energy Fuels* **2021**, *35* (9), 8321−8333.
(55) Wang, C.; Xu, Y.; Wang, X.; Li, L.; Zhang, B.; He, S.; Chen, Y. Insights into the Enhanced Electrochemical Performance of Mn-Deficiency $Li_2Mn_{(1-x)}SiO_4$/C for Li-Ion Batteries: Experimental and Theoretical Study. *J. Power Sources* **2019**, *420*, 46−53.
(56) Wang, C.; Xu, Y.; Sun, X.; Zhang, B.; Chen, Y.; He, S. Enhanced Electrochemical Properties of F-Doped Li_2MnSiO_4/C for Lithium Ion Batteries. *J. Power Sources* **2018**, *378*, 345−352.
(57) Tian, J.; Zhou, X.; Wu, Q.; Li, C. Li-Salt Mediated Mg-Rhodizonate Batteries Based on Ultra-Large Cathode Grains Enabled by K-Ion Pillaring. *Energy Storage Mater.* **2019**, *22*, 218−227.
(58) Du, W.; Zheng, Y.; Liu, X.; Cheng, J.; Chenna Krishna Reddy, R.; Zeb, A.; Lin, X.; Luo, Y. Oxygen-Enriched Vacancy Spinel MFe_2O_4/Carbon (M = Ni, Mn, Co) Derived from Metal-Organic Frameworks toward Boosting Lithium Storage. *Chem. Eng. J.* **2023**, *451*, No. 138626.
(59) Deng, R.; Wang, Z.; Tan, S.; Lu, G.; Huang, X.; Qu, B.; Huang, G.; Xu, C.; Zhou, X.; Wang, J.; Pan, F. Organic Molecular Intercalation Enabled Anionic Redox Chemistry with Fast Kinetics for High Performance Magnesium Storage. *Small* **2024**, *20* (12), No. 2308329.
(60) Dou, S.; Xu, J.; Sari, H. M. K.; Wu, H.-H.; Hu, J.; Zhang, Y.; Fan, L.; Xiong, D.; Zhou, W.; Chen, Y.; Li, X. Large Interlayer Spacing of Few-Layered Cobalt−Tin-Based Sulfide Providing Superior Sodium Storage. *ACS Appl. Mater. Interfaces* **2020**, *12* (37), 41546−41556.
(61) Chen, F.; Zhao, B.; Huang, K.; Ma, X.; Li, H.; Zhang, X.; Diao, J.; Yue, J.; Huang, G.; Wang, J.; Pan, F. Dual-Defect Engineering Strategy Enables High-Durability Rechargeable Magnesium-Metal Batteries. *Nano-Micro Lett.* **2024**, *16* (1), 184.
(62) Yao, Z.; Yu, Y.; Wu, Q.; Cui, M.; Zhou, X.; Liu, J.; Li, C. Maximizing Magnesiation Capacity of Nanowire Cluster Oxides by Conductive Macromolecule Pillaring and Multication Intercalation. *Small* **2021**, *17*, 2102168.
(63) Deng, R.; Lu, G.; Wang, Z.; Tan, S.; Huang, X.; Li, R.; Li, M.; Wang, R.; Xu, C.; Huang, G.; Wang, J.; Zhou, X.; Pan, F. Catalyzing Desolvation at Cathode-Electrolyte Interface Enabling High-Performance Magnesium-Ion Batteries. *Small* **2024**, *20*, 2311587.
(64) Zheng, Y.; Yao, Z.; Shadike, Z.; Lei, M.; Liu, J.; Li, C. Defect-Concentration-Mediated T-Nb_2O_5 Anodes for Durable and Fast-Charging Li-Ion Batteries. *Adv. Funct. Mater.* **2022**, *32*, No. 2107060.
(65) Zheng, Y.; Qiu, W.; Wang, L.; Liu, J.; Chen, S.; Li, C. Triple Conductive Wiring by Electron Doping, Chelation Coating and Electrochemical Conversion in Fluffy Nb_2O_5 Anodes for Fast-Charging Li-Ion Batteries. *Adv. Sci.* **2022**, *9*, No. 2202201.
(66) Peng, C.; Lyu, H.; Wu, L.; Xiong, T.; Xiong, F.; Liu, Z.; An, Q.; Mai, L. Lithium- and Magnesium-Storage Mechanisms of Novel Hexagonal $NbSe_2$. *ACS Appl. Mater. Interfaces* **2018**, *10* (43), 36988−36995.
(67) Ding, S.; Dai, X.; Tian, Y.; Song, B.; Wang, L.; Li, G.; Li, S.; Huang, J.; Li, Z.; Meng, A. Insight into the Coordinating Mechanism of Multi-Electron Reaction and Structural Stability Induced by K^+ Pre-Intercalation for Magnesium Ions Batteries. *Nano Energy* **2022**, *93*, No. 106838.
(68) Ding, S.; Dai, X.; Li, Z.; Wang, C.; Meng, A.; Wang, L.; Li, G.; Huang, J.; Li, S. PVP-Induced Synergistic Engineering of Interlayer, Self-Doping, Active Surface and Vacancies in VS_4 for Enhancing Magnesium Ions Storage and Durability. *Energy Storage Mater.* **2022**, *47*, 211−222.

https://doi.org/10.1021/acs.nanolett.4c04908
Nano Lett. XXXX, XXX, XXX−XXX